Langmuir

Article

pubs.acs.org/Langmuir

# Geometrical and Electrical Properties of Indium Tin Oxide Clusters in Ink Dispersions

Mateusz Sikora,[†,*] Dieter Adam,[‡] Piotr M. Korczyk,[§,⊥] Anna Prodi-Schwab,[‡] Piotr Szymczak,[∥] and Marek Cieplak[†]

[†]Institute of Physics, Polish Academy of Sciences, Aleja Lotników 32/46, 02-668 Warsaw, Poland

[‡]Evonik Industries AG, Paul-Baumann-Strasse 1, 45772 Marl, Germany

[§]Institute of Fundamental Technological Research, Polish Academy of Sciences, ul. Pawińskiego 5B, 02-106 Warsaw, Poland

[⊥]Institute of Physical Chemistry, Polish Academy of Sciences, ul. Kasprzaka 44/52, 01-224 Warsaw, Poland

[∥]Institute of Theoretical Physics, Faculty of Physics, University of Warsaw, ul. Hoża 69, 00-681 Warsaw, Poland

**ABSTRACT:** The analysis of the TEM images of indium tin oxide (ITO) clusters in ink solutions deposited from ink dispersions reveals that their geometry arises from a diffusion limited cluster aggregation (DLCA) process. We model films of ITO clusters as built through deposition of DLCA clusters made of primary spherical nanoparticles of 13 nm in diameter. The deposition is then followed by a further compactification process that imitates sintering. We determine the conductivity of the sintered films by mapping the problem to that of the resistor network in which the contact regions between the touching spheres provide the dominant electric resistance. For a given volume fraction, conductivity of the sintered films is shown to be larger than that for the randomly packed spheres. However, the larger a typical radius of gyration of the clusters the smaller the enhancement. We also provide numerical tests for the routines used in the interpretation of the TEM images.

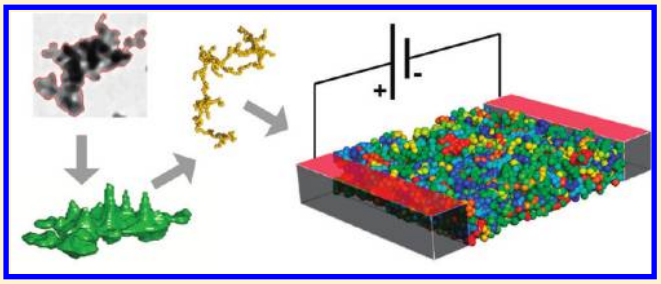


## INTRODUCTION

Transparent conductive oxides serve as electrodes in flat-panel display devices (to control orientation of liquid crystals)[1] and in photovoltaics (to tap photogenerated carriers).[2] Their remarkable properties stem from the wide gap character of the electronic band structure combined with the doping-induced metallic-like electric conduction. Such systems are typically employed in the form of thin films and their examples include ZnO doped with Al or Ga,[3,4] $SnO_2$ doped with F or Sb,[4] and CdO doped with Y, Sc, or In.[5] However, $In_2O_3$ doped with Sn (ITO, indium tin oxide) with a doping level of order 5−10 at. % appears to have superior optical transmittivity in the visible range and the smallest resistivity in the set.[6,7] In addition, ITO reflects the infrared light so it can also function as a heat filter.[8] ITO is an n-type semiconductor with the bixbyite crystal structure and the carrier density of order $10^{21}$ $1/cm^3$ comes from two different kinds of donors (O vacancies and Sn substituting In).[9]

There are many well established methods of layer deposition that enable production of thin ITO films (see references in, e.g., ref 10). They involve vacuum techniques, advanced apparatus, and elevated temperatures. The latter feature is an obstacle when dealing with flexible polymeric substrates which is one of many motivations, including achieving reduction in the manufacturing costs, to explore novel ways of production of the ITO films. A promising new method involves making dispersion, or "inks", of ITO nanoparticles which are suitable for wet deposition techniques, such as spin- and dip-coating and printing.[11,10] Scratch resistant acrylic coatings have also been developed commercially by Evonik-Industries.[12] The nanoparticles themselves are made by the sol−gel technique.[13] There have also been reports on using the inkjet printed films in solar cells.[14,15]

Here, we analyze and then model the properties of nanoparticles in ink formulations designed by Evonik Industries[15,16] for usage in printable electronics. These formulations are water or ethanol based and they contain a dispersant. They are stable and contain particles of about 100 nm in size. Each of the particles is an agglomerate of primary nanoparticles which are about 13 nm in diameter. The primary nanoparticles are crystalline in structure. We show that the agglomerates are fractals[17] with the fractal dimensionality, $d_f$, of about 1.80. We interpret this value as being consistent with the process of diffusion limited cluster aggregation (DLCA)[18−20] in which both the growing clusters and the primary particles move in space and aggregate. We then model the formation the ITO clusters as DLCA-like aggregation of clusters composed of hard spheres and analyze the statistical properties of the aggregates. The diameter of a sphere is taken as equal to 13 nm to imitate properties of the Evonik ink formulation.

**Received:** October 3, 2011
**Revised:** November 28, 2011
**Published:** December 2, 2011

   dx.doi.org/10.1021/la203886b | *Langmuir* 2012, 28, 1523−1530

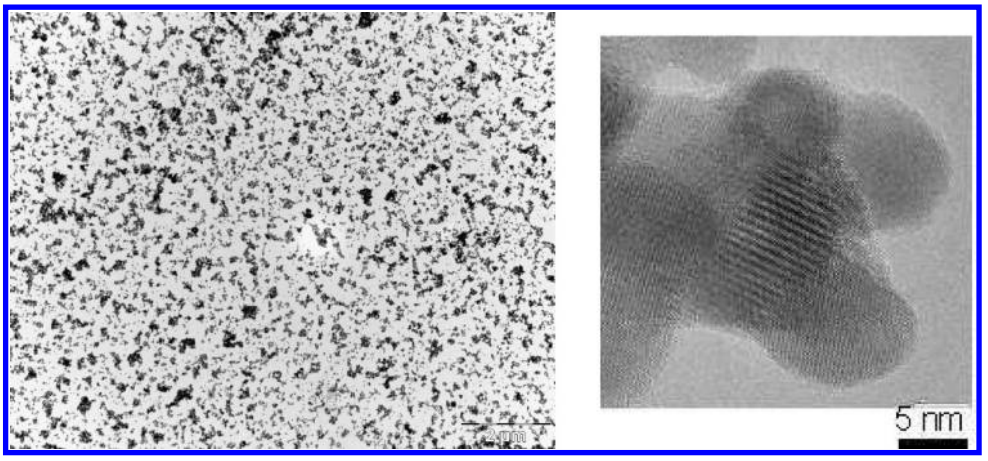


**Figure 1.** Left panel: a TEM image of the ITO clusters deposited from ink dispersion PH37384 in test US12 (frame 56342). Right panel: The highly magnified TEM image of a primary ITO particle.

In the next technological step for the systems considered here, the formulation is inkjetted onto a glass (or plastic) substrate and dried. Further postprocessing involves sintering at 550 °C and then at 300 °C in reducing atmosphere (5%$H_2$ and 95% $N_2$). This results in a layer of 0.5−2.0 $\mu$m, roughness of 10 nm rms, porosity of 35−45% and sheet resistance of about 100 Ω/sq. The optical tranmittance is 90%. The mobility and carrier density in nanoporous ITO films have been measured and discussed in ref 21. In this paper, we model the sintered films by implementing compactification of the hard sphere clusters and then study the resulting resistivities as a function of the characteristic cluster size and porosity.

## ■ ANALYSIS OF CLUSTER IMAGES

Figure 1 shows an example of a transmission electron microscopy (TEM) image resulting from ITO ink deposition on a glass substrate. The right panel shows an image of a primary ITO particle. The particle has crystalline features yet it is fairly compact. Thus, at the length scales of the ITO clusters the particle can approximately represented by a sphere. Our task at hand is to interpret such images through image processing in terms of single cluster geometrical characteristics. There is a substantial collective experience in analyzing TEM images of agglomerated particles that has been accumulated in the literature.[22,24,25,29,30] We follow the developed techniques, combined with using the Matlab Image Processing Toolbox to retrieve data on image brightness from the TEM images. The image is divided into pixels. The linear pixel size is either 9.5, or 4.7, or 1.9 nm, depending on the magnification level of a specific image.

We have used a simple threshold based approach to distinguish clusters from the background on the images. The threshold value is chosen to be equal to the median brightness level across whole image. The pixels with the brightness falling bellow the median are considered as belonging to the clusters. This procedure generates a logical mask image which is then partitioned into clusters of connected pixels. Once the clusters are identified, we proceed to analyzing distribution of brightness corresponding to individual clusters in the TEM images.

The brightness level, $I(x,y)$, of a pixel at location $(x,y)$ depends on the projection of a 3-dimensional structure (Figure 2) on the plane of the substrate as it originates from the transmission of the electron beam through the cluster along the

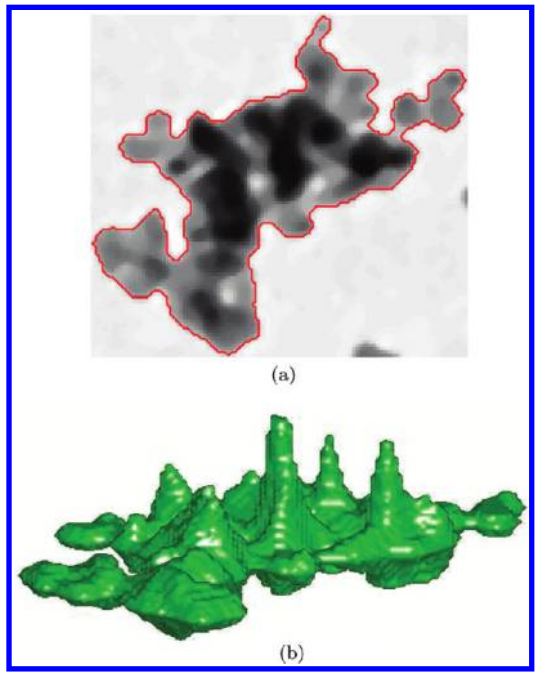


**Figure 2.** Top: the light transmission pattern corresponding to one of the clusters present in Figure 1. Bottom: its 3-dimensional reconstruction.

$z$-axis. $I(x,y)$ does not contain a full information about the structure of a cluster, but this is the only information available experimentally. According to the Lambert−Beer law known in optics, we can expect that $I(x,y)$ depends on the total depth of the cluster at $(x,y)$ exponentially:

$$I(x, y) = I_0 \exp\left( - \frac{l(x, y)}{\alpha} \right) \quad (1)$$

Here $I_0$ denotes the brightness of incident beam and $\alpha$ is the absorption length. We assume that both of these parameters are constant. Furthermore, we assume that $I_0$ is given by the brightness of the background, as estimated by the median value of the brightness. Equation 1 implies that the depth of a layer can be evaluated from digital image by


dx.doi.org/10.1021/la203886b | Langmuir 2012, 28, 1523−1530

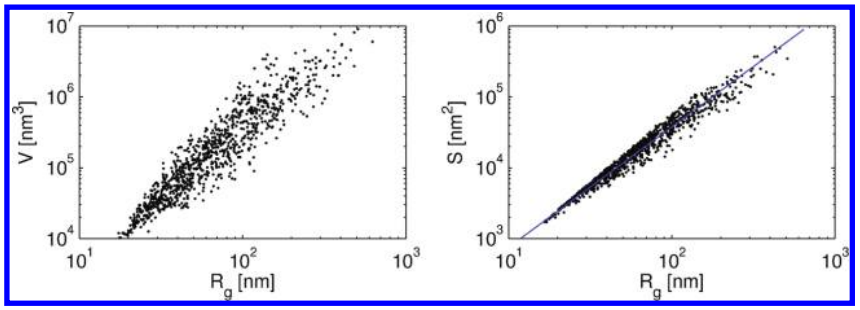


**Figure 3.** Left panel: volume, $V$, of the clusters versus $R_g$ obtained for the set of clusters corresponding to the TEM image shown in Figure 1. Right panel: Surface area of the projections of the clusters considered in the left panel versus $R_g$. The indicated slope correponds to 1.77.

$$l(x, y) = -\alpha \ln\left(\frac{I(x, y)}{I_0}\right) \tag{2}$$

The $\alpha$ coefficient is evaluated from a series of measurements of the smallest objects—the primary nanoparticles. Assuming that the crystallites are spherical, their depth is statistically equal to their width. By measuring the brightness at the center of a crystallite and its width, we estimate $\alpha$ to be equal to 2.22 ± 0.34 nm.

The volume of a cluster can be evaluated by:

$$V = w^2 \sum_{x,y} l(x, y) \tag{3}$$

where $w$ denotes the height and width of a square pixel. The sum extends over all $(x,y)$ pixel positions belonging to the cluster. The volume can also be expressed by a nondimensional number $N$ by dividing it by a volume, $w^3$, of a single voxel

$$N = \frac{V}{w^3} = \sum_{x,y} \frac{l(x, y)}{w} \tag{4}$$

The effective number, $n(x,y)$, of occupied voxels at $(x,y)$ is given by $n(x,y) = (l(x,y))/(w)$. An analysis of the TEM images allows us to determine $n(x,y)$ but the information about the distribution of the occupied voxels along the $z$ axis is not available.

The aim of analysis of the TEM images is to determine the relation between volume of a cluster and its radius of gyration, $R_g$, defined as

$$R_g{}^2 = \frac{1}{N} \sum_{x,y,z} ((x - x_0)^2 + (y - y_0)^2 + (z - z_0)^2) \tag{5}$$

where $(x_0y_0z_0)$ denotes the center of mass of the cluster. Note that $x_0=(1/N)\sum_{x,y}l(x,y)/(w)$ and similarly for the $y$ component. Thus

$$R_g{}^2 = \frac{1}{N} \sum_{x,y} \frac{l(x, y)}{w}(x - x_0)^2 + \frac{1}{N} \sum_{x,y} \frac{l(x, y)}{w}(y - y_0)^2 + \frac{1}{N} \sum_{x,y,z} (z - z_0)^2 \tag{6}$$

The last term in eq 6 cannot be estimated from the images. However, we can assume that, statistically, the clusters are isotropic and estimate the last term as an average of the remaining terms and hence

$$R_g^2 = \frac{3}{2}\frac{1}{N} \sum_{x,y} \frac{l(x, y)}{w}((x - x_0)^2 + (y - y_0)^2) \tag{7}$$

Our analysis basically follows the steps taken in refs 22, 24, 25, 29, and 30, with one important difference. Instead of the linear relation between the effective depth of the clusters and the corresponding darkness of the images, we adopt the Lambert−Beer law which seems to have a much better grounding in the physics of light transmission. It should be noted that our approach still does not take into account effects coming from refraction and scattering. Such effects reduce estimates of depth of the clusters. Furthermore, the assumed cluster isotropy my be invalidated by the presence of the substrate surface. However, the ITO clusters are not grown on the substrate but instead are deposited onto it. We thus expect that anisotropies, if any, should be minor. We should note that TEM micrographs are often quite noisy. Novel ways of dealing with such noise are discussed in ref 28.

The left panel of Figure 3 shows the $V-R_g$ scatter plot (combined from three images) for about a thousand of the ink clusters on the log−log scale. The effective slopes are quite scattered and they vary between 1.87 and 2.30. However, the inaccuracies of the method are significantly reduced when one plots the total surface, $S$, of the projection of the cluster on the surface of the image vs $R_g$. The right panel of this figure shows shows that the $S-R_g$ dependence is well-defined and can be fitted by the power law with the exponent $d_f$ = 1.77 ± 0.08, which is interpreted as a fractal dimension of this two-dimensional shadow. Such a planar fractal dimensionality can, in general, be distinct from the fractal dimensionality of the original three-dimensional cluster.[23] In this case, however, the two dimensionalities coincide. As elaborated by Mandelbrot,[17] when one projects a fractal object—originally embedded in the three-dimensional space—onto a plane, then the projection's fractal dimension is given by $d_{fp} = \min(d_f,2)$. In our case, $d_{fp}$ is indeed smaller than 2 so we conclude that $d_f = d_{fp}$.

It is important to realize that the value of $d_f$ we get is fully consistent with the range of values (1.75−1.80) obtained in three-dimensional simulations of the DLCA growth process[18−20] in the so-called flocculation regime in which the particle number concentration is low and separations between various clusters are large. The difference between the DLCA and DLA[26,27] processes is that in DLA, individual particles are allowed to diffuse until they collide with a single immobilized cluster, while in DLCA, all particles and clusters in the systems diffuse and collide to form clusters and compound clusters. It is interesting to note that diffusion of nanoparticles may be affected by other effects, such as dipole−dipole interactions


dx.doi.org/10.1021/la203886b | Langmuir 2012, 28, 1523−1530

invoked in the context of soot particles[23,31] to explain $d_f$ of 1.51 instead of 1.80.

## MODELING OF THE ITO CLUSTERS IN TERMS OF HARD SPHERES

Modeling the formation of the ITO ink nanoparticles in atomic detail is difficult. Instead, we propose to use a coarse-grained model in which the primary nanoparticles are hard spheres (of radius, $R_{NP}$, equal to 6.5 nm) which aggregate together on coming within a gap distance of less than 0.5 nm. The process is considered to be irreversible. Once the spheres come to within such binding distance, their relative motion is arrested. For simplicity, we consider the spheres to be monodisperse. Since the experimental findings are consistent with the DLCA growth process, the Brownian motion of the nanoparticles in the solution can be described as a Monte Carlo process. We use the cell list algorithm[32] in which the periodic simulation box is partitioned into a number of small cells in such a way that only particles from 26 neighboring cells can collide. For the hard sphere case considered here, it is convenient to set the linear cell size equal to $R_{NP}$. In each Monte Carlo step, a particle is picked at random and then is subjected to a tentative random displacement. The displacement is accepted if the energy of the system is not raised, i.e., if it generates no overlap between the spheres. Note that the hard sphere system comes with no temperature that could be associated with it.

The time scales of translational motion are set by diffusivity of the nanoparticles. A single step in the movement of the primary nanoparticle involves a random displacement of between 0 and $\delta x$ in a random direction and no rotation. We set $\delta x$ to 1 nm. Once two or more nanoparticles form a cluster, rotational motion is also possible. For a dimer, the rotational angle is selected between 0 and 10° randomly. The rotation axis is also selected randomly. We scale the movement of clusters to account for the decrease of their mobility with size. The rotational angle scales as $S^{-1/2}$, where $S$ is the number of particles in a cluster. The translational motion scales as $S^{-2/3}$.[33] In our approach, we model the formation of the aggregates dynamically, which is quite distinct from the one considered by Peukert and his collaborators.[34,35] They first generate small clusters in a stochastic way. In the next step, they select two clusters, rotate them by random angles and then move their centers of mass toward each other until the clusters meet. The advantage of their approach is that it allows for a rapid construction of large clusters.

Our studies pertain to three technological stages in the production of the ITO films. Stage I is the preparation of the cluster containing ink. Stage II is the deposition of the ink onto a substrate. Stage III is the compactification, drying, and sintering of the film which results in the final product.

**Stage I.** The clusters form under the conditions of flocculation—in a relative dilution. We achieve these conditions by considering a simulation box of 1600 × 1600 × 6000 nm$^3$ and 691200 primary particles. The periodic boundary conditions are employed to provide conditions which are appropriate for an isotropic growth. We evolve the system until the mean value of $R_g$, $\langle R_g \rangle$, acquires predefined values: 25, 50, 80, and 100 nm. The latter value is as in the actual experiments. An example of a typical cluster formed is shown in Figure 4. Its dendritic appearance is consistent with $d_f$ 1.80 and thus with the DLCA-like erowth. The size distribution of the clusters obtained at this stage, as measured by $R_g$, is shown in the bottom panel of Figure 5. The top panel of this figure is a cross

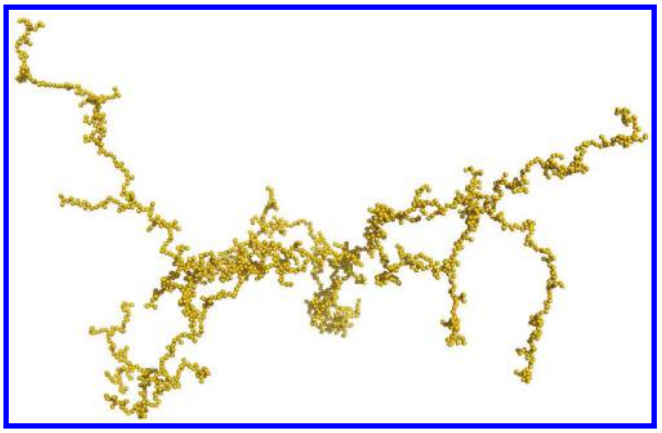

**Figure 4.** Example of a DLCA cluster obtained through simulations. Its $R_g$ corresponds to about 100 nm.

plot showing $S$ against $R_g$ on the log−log scale for each cluster in the system. In this case,$\langle R_g \rangle$ is close to 40 nm, the median value is 35 nm, and the largest cluster has $S$ = 924. The relationship is consistent with $d_f$ = 1.80.

**Stage II.** Once the clusters are grown, we replace the periodic walls by confining walls in an adiabatic fashion. This is implemented by imposing a slight force that directs clusters that cross boundaries toward the inside of the simulation box. Once this is accomplished, the walls are set to be rigid and flat. At the same time we switch on a gravitational bias which pushes the clusters toward the substrate at the bottom, i.e. down the $z$-axis. This step imitates the printing stage of the technological process. The system is evolved until the average value of the center of mass of the system, $\langle z_{cm} \rangle$ starts to vary insignificantly. An example of the resulting depositional configuration is shown in Figure 6.

When calculating the conductivity of the printed films, one needs to know which spheres form an electric contact. The spheres are just models of the crystalline primarily nanoparticles whose surface roughness is varying on the scale of a lattice constant. The elementary cell of the bixbyite ITO lattice consists of two diagonally linked cubes with the total edge length of about 1.02 nm.[36] Thus, two spheres are considered as making a contact if their gap distance is less than 1 nm (i.e., the effective radius of the sphere is 7 nm instead of 6.5 nm associated with the core).

**Stage III.** In the final stage, we induce compactification by applying external force oscillations along the three Cartesian directions simultaneously, combined with a steady downward pushing of magnitude $g$. The period of the oscillations is 1000 Monte Carlo steps. The oscillations in the $z$-direction vary between $-g$ and $+0.1g$. In the remaining directions − between $-0.1g$ and $+0.1g$. The system is evolved until the period averaged $\langle z_{cm} \rangle$ ceases to vary in any significant manner. The shaking of the system allows the clusters to get rid of accidentally trapped overhanging configurations and thus come closer together. The packing effects of compactification are illustrated in Figure 7 for a system of 77760 primary nanoparticles and$< R_g >$ close to 25 nm. In the bottom slice of width 100 nm, the volume fraction of the ITO material is 0.251. On compactification it becomes 0.354. A close-up of cluster configurations before and after compactification for$<R_g>$ = 50 nm is shown in Figure 8. The clusters are seen to get immobilized through steric hindrances. The hindrances are reduced on shaking combined with further compactification.


dx.doi.org/10.1021/la203886b | Langmuir 2012, 28, 1523−1530

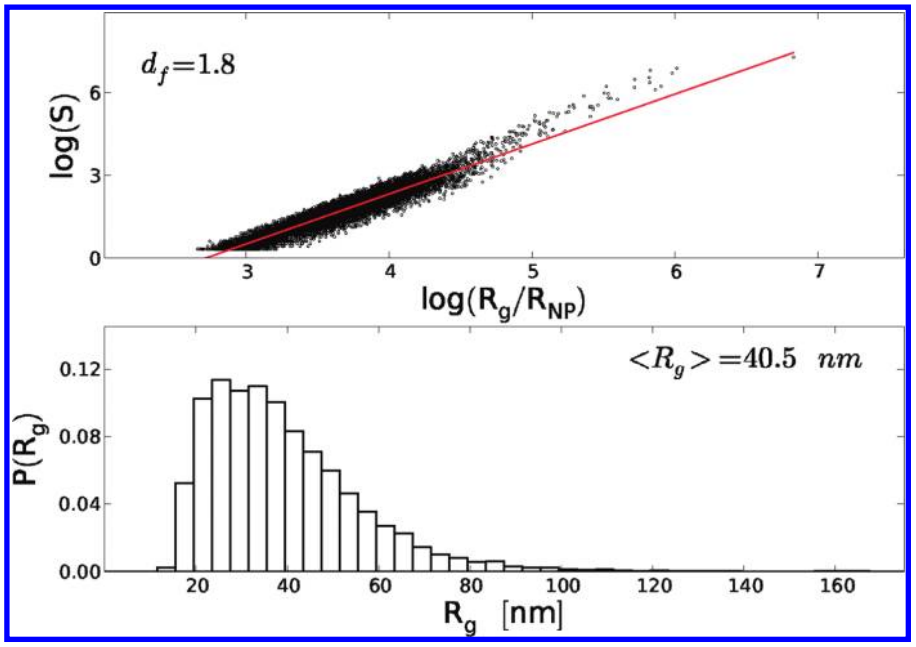


**Figure 5.** Top panel: the relationship between $R_g$ and the number of primary nanoparticles in the cluster. Bottom panel: the corresponding distribution of the values of $R_g$.

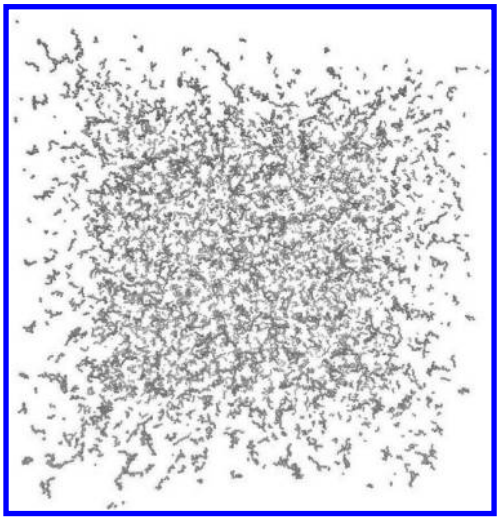

**Figure 6.** Top view of a printed configuration corresponding to $\langle R_g \rangle$ = 100 nm.

In order to imitate sintering,[34] we assume that the heat treatment increases the surface roughness and thus allows for electric contacts which are broader ranged: the contact is considered established when the gap distance does not exceed 1.5 nm.

## TESTS OF THE IMAGE RECONSTRUCTION PROCEDURE

We can now use the DLCA-generated clusters for tests of our methods of interpretation of the TEM images. The way to do it is illustrated in Figure 9 for four nonconcentric spherical particles located above a point $(x,y)$ (meaning that this point is within a "shade" region of each particle). We first define a "shade function"

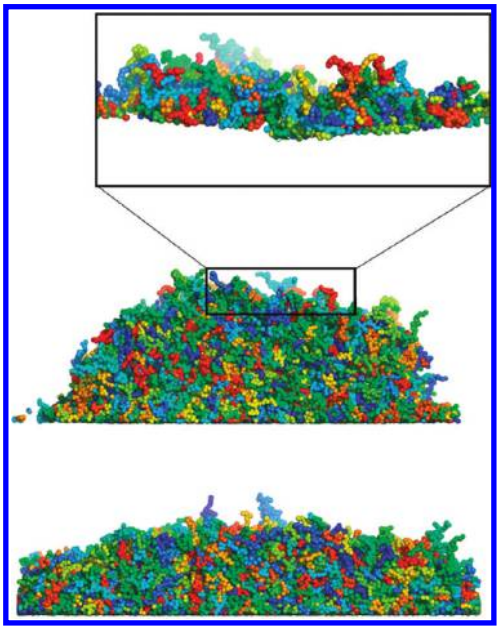

**Figure 7.** System configuration corresponding to $\langle R_g \rangle$ = 25 nm. The middle panel shows the system obtained upon the gravitational collapse. The top panel shows its magnified fragment. The bottom panel shows the compactified system obtained through vibrations. The variety of colors used serves to identify individual clusters.

$$S(x, y, i) = \begin{cases} 0 & \text{if } (x - x_{0i})^2 + (y - y_{0i})^2 \geq R_i \\ 1 & \text{if } (x - x_{0i})^2 + (y - y_{0i})^2 < R_i \end{cases} \quad (8)$$

where $R_i$ denotes a radius of the $i$th particle and $(x_{0i},y_{0i})$—the planar position of its center. Adding such $S(x,y,i)$ terms over the $n$ particles would generate a sharply delineated projection on the substrate in all places where $\sum_i^n S(x,y,i)$ is nonzero. The


dx.doi.org/10.1021/la203886b | Langmuir 2012, 28, 1523−1530

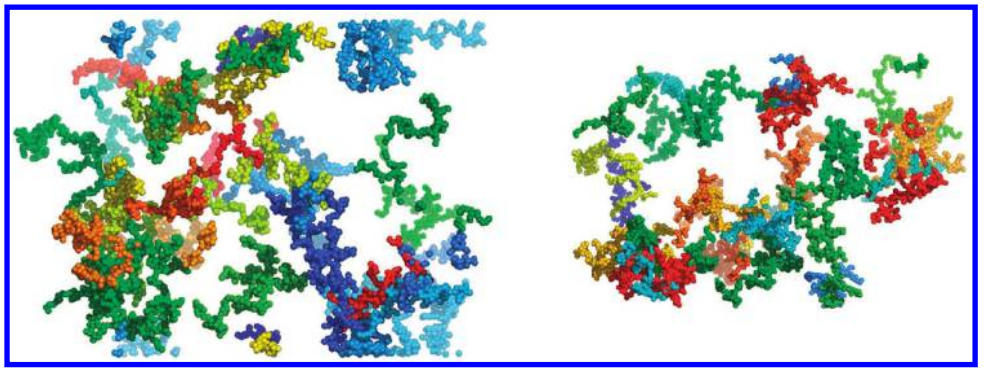

**Figure 8.** Close-up of the system's configuration corresponding to $\langle R_g \rangle$ = 50 nm. The left panel shows a set of clusters obtained through the gravitational collapse. The clusters shown get stuck mechanically and form a ring. Smaller clusters within the ring are not shown. The right panel shows the same system after compactification.

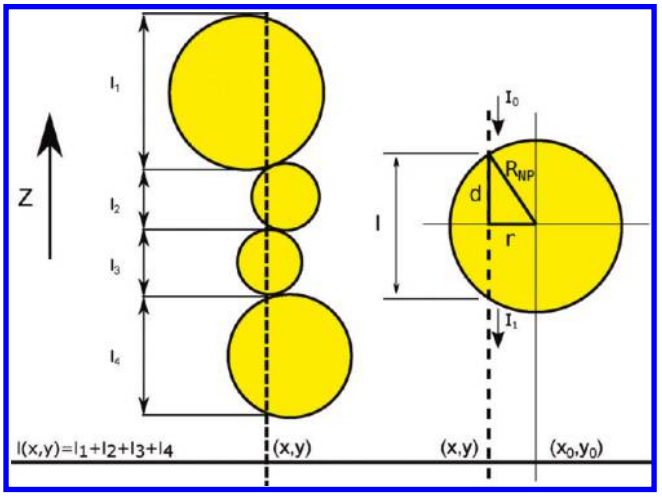


**Figure 9.** Schematic representation of a generation of a TEM-like image by four spherical particles.

resulting intensity pattern would vary in discrete steps. Instead, we want to mimick the thickness-related absorption to get more gradually varying "brightness" level across the pattern which would be consistent with the Lambert−Beer law as in eq 1. The procedure used is illustrated in Figure 9. If the incident intensity is $I_0$ then, on passing through the four spheres shown, it becomes $I = I_0 \exp((l_1 + l_2 + l_3 + l_4)/\alpha))$, where $l_i = 2(R_{NP}^2 - r_i^2)^{1/2}$ and $r_i^2 = (x - x_{0i})^2 + (y - y_{0i})^2$. For our tests then, the whole shaded region gets modulated brightness in accordance with the exponential decay.

The central part of Figure 10 shows an example of a computer generated DLCA cluster of $R_g$ = 200 and $S$ = 447. The upper right corner represents the corresponding intensity pattern on the $x,y$ plane obtained using the Lambert−Beer law as just discussed. The bottom panel shows the reconstruction of the cluster based on the intensity pattern. We conclude that the reconstruction is reasonably related to the original and thus our inference about the DLCA-like character of the ITO clusters stemming from our analysis of the TEM images is solid.

## ■ CONDUCTIVITY OF THE SINTERED FILMS

To assess the influence of cluster size and sintering on the electrical transport of the DLCA films we determine the conductivity in a setup shown in the left panel of Figure 11. We treat the system as a resistor network with particle centers being nodes and interparticle contacts being resistors. Two

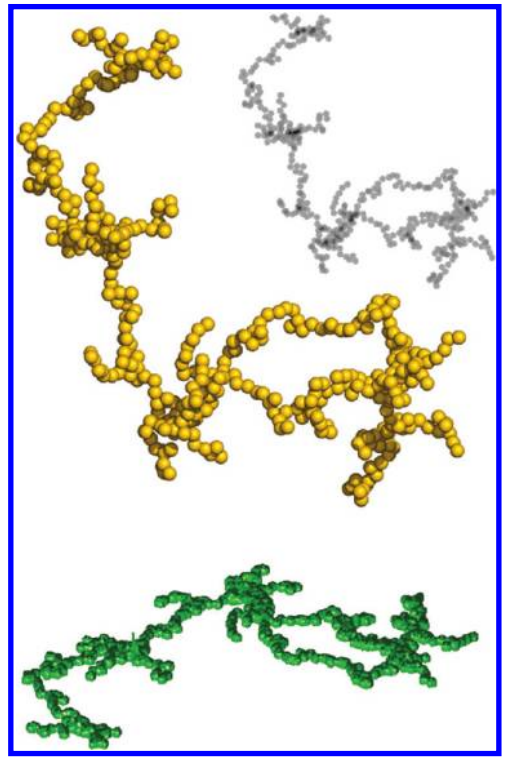

**Figure 10.** Testing the methods of the image reconstruction for a computer generated DLCA cluster, as explained in the text. The reconstruction is seen from the [011] perspective whereas the original cluster is seen from the [0,0,−1] perspective. The change in the perspective gives a better grasp of the structure.

approximations are made here: first, we assume that the interparticle resistance is arises primarily in the contacts at particle surfaces. Second, all the contact resistances are assumed to be uniform, of magnitude $R$. The value of $R$ is difficult to assess. A model discussed in ref 35 appears to suggest that $R$ can be of order 100 Ω at the room temperature. However, unlike what is considered in that model, we assume that the resistance of the system is dominated by the contacts due to their narrow geometry.

In order to reduce effects related to the rough boundaries of the system, we consider cutout blocks of $L_x \times L_y \times L_z$ that are mounted on the substrate, as illustrated in Figure 11. Each of these Cartesian lengths should be taken as being smaller than the corresponding system size and yet much bigger than $\langle R_g \rangle$ of the clusters. We imagine that a potential difference, $V$, is


dx.doi.org/10.1021/la203886b | Langmuir 2012, 28, 1523−1530

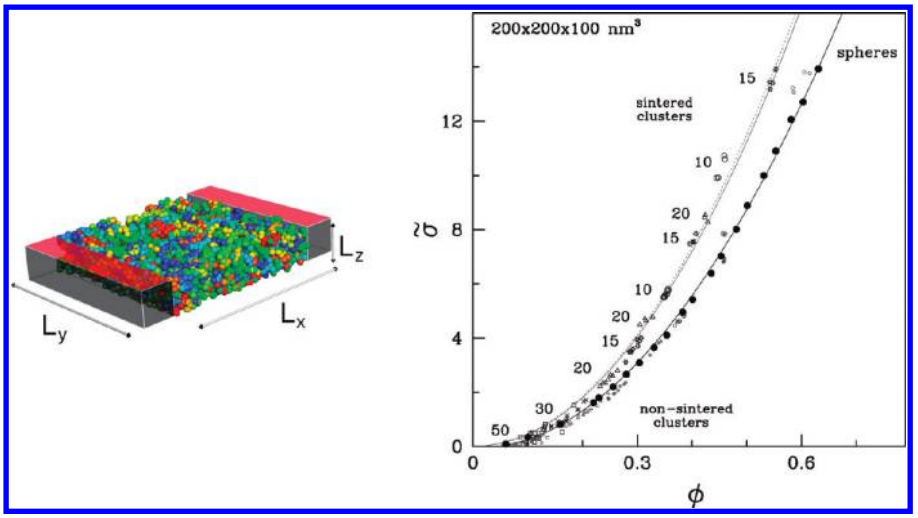


**Figure 11.** The left panel: example of a configuration of the simulated sintered film with $\langle R_g \rangle$ = 25 nm placed between two planar electrodes. Various clusters come with various colors. The geometrical parameters of the cut-out are: $L_x = L_y$ = 500 nm and $L_z$ = 100 nm. The full simulational box has the planar dimensions of 1800 by 1800 nm. The right panel:dimensionless conductivity as a function of the volume fraction in a layer of area 200 × 200 nm$^2$ and width 100 nm. The solid circles correspond to randomly packed spheres of radius $R_{NP}$ that fell on the substrate gravitationally without any compactification. The data points can be fitted to a parabolic line: $\tilde{\sigma} = b + a\varphi^2$, where $b = -0.109$ and $a = 35.41$ as indicated. The percolation threshold is thus at $\phi = 0.056$ and below this threshold the system is insulating. All other symbols correspond to systems of clusters with the indicated values of $\langle R_g \rangle$ in nm. The smaller and fainter symbols correspond to the systems before sintering. The larger symbols refer to systems after sintering. The data points for the sintered system are fitted to a parabolic line: $\tilde{\sigma} = b + ax^2$, with $a = 45$ and $b \sim 0$ (a large scattter of data around $x = 0$ does not allow us to reliably determine the percolation threshold in this case). When systems of width 150 nm are considered (the data points are not shown for clarity of the figure) the results are changed only slightly—the best fit to the data points is shown by the dotted line and it corresponds to $a = 46$.

applied at the electrodes mounted on the first and last faces of the block when viewed in the $x$-direction. As a result, a current, $I$, flows through the system. The electrical conductivity, $\sigma$, for such a block is defined by the relation $\sigma = i/E$, where $i$ is the current density and $E$ is the electric field. The current density can be expressed as $i = I/L_yL_z$ whereas the field $E = V/L_x$. Thus

$$\sigma = IL_x/VL_zL_y \tag{9}$$

In view in the uncertainty in the value of $R$, it is more convenient to work with dimensionless conductivity, $\tilde{\sigma}$, defined as $\tilde{\sigma} = \sigma R_{NP}R$.

The problem of determining $\tilde{\sigma}$ is then reduced to the question of finding the equivalent resistance of a resistor network, in which a certain group of nodes (the ones which are closer to the $x = 0$ surface than $R_{NP}$) is at the voltage $V$, whereas another group (the ones closer to the $x = L_x$ surface than $R_{NP}$) is grounded. As we have discussed previously, the approximate criterion for two nodes to form a contact depends on whether the films are considered sintered or not. In the former case, a contact is considered to arise if the gap distance between two spheres is less than 1.5 nm, i.e., if the distance between the centers of two spheres is smaller than $2R_{NP}a$, where $a$ = 1.11 (before sintering, $a$ = 1.08). The resistance problem is then obtained using the SPICE software[37] which solves Kirchoff equations for all particle contacts in the system.

We determine $\tilde{\sigma}$ for the nanoparticle systems corresponding to various $\langle R_g \rangle$. In particular, we consider the case of solitary nonaggregated spheres when $\langle R_g \rangle = R_{NP}$. For each system, we select several bottom cut-outs in configurations such as shown in Figure 11. The cut-outs are of size 200 nm × 200 nm × $w$, where $w$ is either 100 or 150 nm. For the systems of clusters, we compare $\tilde{\sigma}$ obtained before sintering and after sintering in order to assess the impact of such processing. Each system is characterized by the volume fraction, $\phi$, that the primary nanoparticles take in the cut-out block (and as determined after the compactification).

The right panel of Figure 11 shows $\tilde{\sigma}$ vs $\phi$ for various arrangements of randomly packed spheres and for many cluster systems corresponding to $\langle R_g \rangle$ of 10, 15, 20, 30, and 50 nm. The conductivity of the randomly packed spheres follows a parabolic dependence on $\phi$. However, for $\phi$ below ~0.056, there is not enough connectivity in the system to provide percolation and the system is insulating.

Note that due to the stochastic character of the process of gravitational deposition and sintering, a system of clusters with a given value of $\langle R_g \rangle$ may end up, after the deposition, in states with different values of $\phi$. In particular, $\langle R_g \rangle$ of 15 nm may have $\phi$ both smaller and larger than systems with the $\langle R_g \rangle$ of 10. However, the general tendency is that the larger the $\langle R_g \rangle$, the smaller the corresponding range of the values of $\phi$. Furthermore, when all sets of data are taken together then a parabolic dependence on $\phi$ is observed. It should be noted that the parabolic dependence of conductivity on $\varphi$ in the systems of spheres and clustered spheres is in contrast with the exponentially varying conductivity found, for instance, in sputtered GeAl cermets.[38,39] At low temperatures, Ge acts as an insulating component in the cermets.

Sintering increases the conductivity in a noticeable manner and the parabolic dependence gets steeper. (It should be noted that an actual sintering process involves chemical processes which go beyond a mere adjustment in the cluster relative positioning and other geometrical features.) Our results indicate that a much more substantive increase in conductivity could be obtained by working with clusters with smaller values of $\langle R_g \rangle$ than ~100 nm considered currently. This would also mean working at larger volume fractions and thus bigger weights.


dx.doi.org/10.1021/la203886b | Langmuir 2012, 28, 1523−1530

## ■ ACKNOWLEDGMENTS

This work has been supported by the EC FUNMOL project under FP7-NMP-2007-SMALL-1, and by the European Union within European Regional Development Fund, through Innovative Economy Grants (POIG.01.01.02-00-008/08 and NanoFun POIG.02.02.00-00-025/09). P.S. acknowledges support by the Foundation for Polish Science (FNP) through TEAM/2010-6/2 project cofinanced by the EU European Regional Development Fund.

## ■ REFERENCES

(1) Chopra, K. L.; Major, S.; Pandya, D. K. *Thin Solid Films* **1997**, *102*, 1.
(2) Ohta, H.; Hosono, H. *Mater. Today* **2004**, *7*, 42.
(3) Lin, D.; Wu, H.; Pan, W. *Adv. Mater.* **2007**, *19*, 3968.
(4) Minami, T. *Semicond. Sci. Technol.* **2005**, *20*, S35.
(5) Yang, Y.; Jin, S.; Medvedeva, J. E.; Ireland, J. R.; Metz, A. W.; Ni, J.; Hersam, M. C.; Freeman, A. J.; Marks, T. J. *J. Am. Chem. Soc.* **2005**, *127*, 8796.
(6) Wang, R. X.; Djurisic, A. B.; Beling, C. D.; Fung, S. H. Y. Indium Tin Oxide (ITO) thin films: Fabrication, properties, post-deposition treatments and applications. In *Trends in Semiconductor Research*; Nova Science Publishers, Inc.: Hauppauge, NY, 2005; Chapter 6, pp 137−174.
(7) Aksu, Y.; Driess, M. *Angew. Chem., Int. Ed.* **2009**, *48*, 7778.
(8) Frank, G.; Kauer, E.; Koestlin, H. *Thin Solid Films* **1981**, *77*, 107.
(9) Hamberg, I.; Granqvist, C. G. *J. Appl. Phys.* **1986**, *60*, R123.
(10) Guenther, G.; Schierning, G.; Theissmann, R.; Kruk, R.; Schmechel, R.; Baehtz, C.; Prodi-Schwab, A. *J. Appl. Phys.* **2008**, *104*, 034501.
(11) Epifani, M.; Diaz, R.; Arbiol, J.; Siciliano, P.; Morante, J. R. *Chem. Matter.* **2006**, *18*, 840.
(12) The A to Z technology website. www.azonano.com/article.aspx?ArticleID=1601 (accessed Sep 16, 2011)
(13) Al-Dahoudi, N.; Aegerter, M. A. *Thin Solid Films* **2006**, *502*, 193.
(14) Krebs, F. C. *Solar Energy Mat. Solar Cells* **2009**, *93*, 394.
(15) Prodi-Schwab, A.; Inhester, M.; Thoelmann, D.; Adam, D. 2009, International Patent Application WO PCT/EP2009/056929.
(16) Hofman, M.; Birnstock, J.; Luethge, T.; Adam, D.; Inhester., M. International Patent Application, WO PCT/EP2007/007673, 2007.
(17) Mandelbrot, B. B. *The fractal geometry of nature*; Freeman: New York, 1983.
(18) Meakin, P. *Phys. Scr.* **1992**, *46*, 295.
(19) Babu, S.; Gimel, J. C.; Nicolai, T. *Eur. Phys. J. E* **2008**, *27*, 297.
(20) Gimel, J. C.; Nicolai, T. *J. Sol-Gel Sci. Technol.* **1999**, *15*, 129.
(21) Gondorf, A.; Geller, A.; Weissbon, J.; Lorke, A.; Inhester, M.; Prodi-Schwab, A.; Adam, D. *Phys. Rev. B.* **2011**, *83*, 212201.
(22) Cai, J.; Lu, N.; Sorensen, C. M. *Langmuir* **1993**, *9*, 2861.
(23) Chakrabarty, R. K.; Garro, M. A.; Garro, B. A.; Chancellor, S.; Moosmueller, H.; Christopher, H. M. *Aerosol Sci. Technol.* **2011**, *45*, 903.
(24) Mustafi, N.; Raine, R. *Aerosol Sci. Technol.* **2009**, *43*, 951.
(25) Shin, W. G.; Wang, J.; Mertler, M.; Sachweh, B.; Fissan, H.; Pui, D. Y. H. *J. Nanopart. Res.* **2008**, *11*, 163.
(26) Witten, T. A.; Sander, L. M. *Phys. Rev. Lett.* **1981**, *47*, 1400.
(27) Meakin, P. *Phys. Rev. Lett.* **1983**, *51*, 1119.
(28) Park, W.; Midgett, C. R.; Madden, D. R.; Chirikjian, G. S. *Int. J. Robotics Res.* **2011**, *30*, 730.
(29) Sorensen, C. M.; Feke, G. D. *Aerosol Sci. Technol.* **1996**, *25*, 328.
(30) Zhang, H. X.; Sorensen, C. M.; Ramer, E. R.; Oliver, B. J.; Merklin, J. F. *Langmuir* **1988**, *4*, 867.
(31) Chakrabarty, R. K.; Moosmueller, H.; Arnott, W. P.; Garro, M. A.; Tian, G.; Slowik, J. G.; Cross, E. S.; Han, J.-H.; Davidovits, P.; Onasch, T. B.; Worsnop, D. W. *Phys. Rev. Lett.* **2009**, *102*, 235504.
(32) Allen, M. P.; Tildesley, D. J. *Computer Simulations of Liquids*; Clarendon Press: Oxford, U.K., 1987.
(33) Sikora, M.; Szymczak, P.; Thompson, T.; Cieplak, M. *Nanotechnology* **2011**, *22*, 445601.
(34) Schmid, H.-J.; Al-Zaitone, B.; Artelt, C.; Peukert, W. *Chem. Eng. Sci.* **2005**, *61*, 293.
(35) Mahajeri, M.; Voight, M.; Klup Taylor, R. N.; Reindl, A.; Peukert, W. *Thin Solid Films* **2010**, *518*, 3373.
(36) Quass, M.; Eggs, C.; Wulff, H. *Thin Solid Films* **1998**, *332*, 277.
(37) Nagel, L. W.; Pederson, D. O. SPICE (Simulation Program with Integrated Circuit Emphasis), Memorandum No. ERL-M382, University of California: Berkeley, CA, 1973; see also en.wikipedia.org/wiki/SPICE/
(38) Deutscher, G.; Kapitulnik, A.; Rappaport, M. *Percolation in metal-insulator systems*; In *Annals of the Israel Physical Society, Percolation Processes and Structures* Deutscher, G., Zallen, R., Adler, J.; Israel Physical Society: Jerusalem, Israel; 1983; Vol *5*, p 207.
(39) McLAchlan, D. S.; Blaszkiewicz, M.; Newnham, R. E. *J. Am. Ceram. Soc.* **1990**, *73*, 2187.